RESEARCH PAPER

Numerical modelling of gassy sand behaviour under monotonic loading

Cheng Chen[1] · Yong Wang[1] · Xianwei Zhang[1] · Lingwei Kong[1] · Guofang Xu[1]

Abstract

The mechanical behaviour of gassy sand is rather complex owing to the inherent complex nature of sand and the occluded/dissolved gas. For better understanding of the behaviour of gassy sand under monotonic loading, a numerical model is presented in this paper. By considering the gas–water mixture in gassy sand as a homogenous pore fluid, the theory of two-phase saturated porous media is employed. Based on this theory, the impact of the occluded/dissolved gas is characterized by the relationship between the compressibility of pore fluid and the degree of saturation as well as the pore fluid pressure, derived from Boyle's and Henry's Laws. Then an advanced constitutive model for sand is combined with the porous media theory to capture the complex stress–strain behaviour of sand, using a single set of model parameters. Through the spatial and temporal discretization of the governing equations by the finite element method and the well-known θ-method, the porous model is numerically implemented as a user-defined element subroutine provided by ABAQUS, in which the implicit constitutive integration algorithm is used. Finally, the influences of gas type, degree of saturation, pore fluid pressure level, and physical state (void ratio and stress level) on the behaviour of gassy sand are studied by the numerical model. The model is validated by comparing the simulated results with laboratory test data from literature.

1 Introduction

As defined by Wroth and Houlsby [29], gassy soil is a class of soil with high degree of saturation (always higher than 85%), in which the liquid phase is continuous while the gas phase is discontinuous in the form of bubbles. Gassy soils are widely distributed in marine, lacustrine, or interactive marine and terrestrial sedimentary environments [6]. The gas, predominately methane, in gas-charged sediments is produced from organic matter in the sediments. Gas may exist in solution in the pore fluid or may be present in its free form. Moreover, the modes of free gas occurrence are different for fine-grained soil and coarse-grained soil mainly due to the relative dimensions of the soil particles and gas bubbles [14, 26]. In this work, the coarse-grained soil is concerned, in which gas bubbles occluded in pore fluid are smaller than the size of soil grain without playing any effect on soil matrix. Compared to water fully saturated sand, the compressibility of gassy sand is higher on account of the high compressibility of the occluded gas. In addition, the variation of pore fluid pressure can make the gas dissolution or exsolution, which would alter the degree of saturation, the compressibility of pore fluid, and consequently influence the mechanical behaviour of soil skeleton [21]. These characteristics, in combination with the dilatancy behaviour of sand, make the mechanical behaviour of gassy sand more complex.

✉ Guofang Xu
gfxu@whrsm.ac.cn

Cheng Chen
cchen@whrsm.ac.cn

Yong Wang
ywang@whrsm.ac.cn

Lingwei Kong
lwkong@whrsm.ac.cn

[1] State Key Laboratory of Geomechanics and Geotechnical Engineering, Institute of Rock and Soil Mechanics, Chinese Academy of Sciences, Xiaohongshan 2#, Wuhan 430071, China

In past decades, a few researchers have investigated the mechanical behaviour of gassy sand by using laboratory testing. Rad et al. [20] conducted a series of undrained triaxial compression tests on gassy dense sand to study the effects of gas type, initial pore fluid pressure, and gas amount. The results indicated that the higher the solubility coefficient of the gas is, or the more gas is occluded, the weaker the specimens may behave under undrained shearing. Furthermore, the lower the initial pore pressure is, the greater the potential for lower strength under undrained shearing. Vega-Posada et al. [22] investigated the effect of gas on the mechanical behaviour of medium-dense sand by performing undrained triaxial compression tests. It was found that the addition of gas, even by small amounts, would lead to a significant reduction of the undrained shear strength of the specimens. Grozic et al. [8] studied the behaviour of gassy loose sand under static undrained triaxial compression conditions and concluded that a reduction in the degree of saturation could induce a decrease in the static liquefaction potential. For a specific void ratio, flow liquefaction will not occur if the degree of saturation is lower than the 'cut-off' value. Similar conclusions are also obtained by He and Chu [11]. In addition, by comparing the results of undrained tests on gassy specimens with the ones of drained effective stress path tests on fully saturated specimens, Finno et al. [5] validated the applicability of the original form of Terzaghi's effective stress principle for gassy sand.

Unlike the plenty of experimental studies on gassy sand, less numerical model is proposed for describing the mechanical responses of gassy sand. Grozic et al. [9] proposed a gassy sand model by combining the sand model developed by Imam et al. [15] with the Hilf's equation [12] that was used to take account of the gas induced properties. In this model, an iterative process was performed to balance the pore fluid pressure change and volumetric strain increment under globally undrained condition. Except the incapability to predict the slight increase in mean effective stress in the initial loading stages, the combined numerical model can well predict the responses of gassy loose sand under undrained triaxial compression conditions. Likewise, the similar method was applied for gassy clay through the replacement of sand model by cam clay model [10]. Nixon and Grozic [19] proposed a simple numerical model to investigate the effect of gas hydrate dissociation on the stability of submarine slope. The result showed that dissociation of even small amount hydrate can cause a significant destabilizing effect. Based on the constitutive model [18] which was obtained by extending the hypoplastic model for sand [25] with the intergranular strain concept, Zapata-Medina et al. [31] suggested a numerical model for gassy sand using the finite element program PLAXIS 2D, in which the pore fluid

compressibility are calculated by the relationship developed by Fredlund [7]. Good consistency was obtained between the undrained triaxial compression test results of gassy medium-dense sand and the corresponding simulations. The undrained mechanical behaviour of gassy sand was also studied by Hong and Xu [13, 30] through using the discrete element method (DEM), where the micro-responses were extensively discussed. The simulations are found to be comparable with the experimental results and/or the theoretical prediction results. Besides, two cases involving gas exsolution were numerically simulated by Mabrouk and Rowe [17] and Dittrich et al. [4], in which the variations of pore fluid compressibility were all considered. Despite the existing studies, the mechanical responses of gassy sand under different conditions, such as gas type, gas amount, and existing form of gas, pore pressure level as well as physical state (void ratio and stress level) of sand, are less comprehensively investigated.

The aim of this paper is to present a numerical model to investigate the mechanical behaviour of gassy sand under monotonic loading. To this end, by considering the pore gas–water mixture in gassy sand as a homogenous pore fluid, the theory of two-phase saturated porous media is employed, in which the compressibility of pore fluid is determined using Boyle's and Henry's Laws. An advanced bounding surface plastic model named SANISAND-Z [3] is added to the porous model to capture the complex mechanical behaviours of sand with the same set of model parameters. Then, the governing equations are spatial and temporal discretized by the finite element method (FEM) and the well-known θ-method. The discretized governing equations are further implemented as a user-defined element (UEL) subroutine in ABAQUS, where the implicit constitutive integration algorithm is used. Finally, the capability of the numerical model is validated by comparing the simulation results with the laboratory data involving different experimental conditions.

2 Methodology

2.1 Governing equations for two-phase saturated porous media under quasi-static condition

In quasi-static condition, slow motion phenomena such as the consolidation behaviour of soils, all acceleration terms in the motion equations become negligible and can be omitted. The overall equilibrium equation of soil-fluid mixture can then be expressed as

$$\sigma_{ij,i} + b_i = 0 \tag{1}$$

The mass conservation of the fluid flow can be written as

$$\alpha \dot{\varepsilon}_{ii} + 1/Q\dot{p}_f = \left(k_{ij}p_{f,j}\right)_{,i} \tag{2}$$

Taking account of the elastoplastic deformation properties of soils, the constitutive law can be expressed in an incremental form:

$$d\sigma_{ij} = d\sigma'_{ij} - \alpha\delta_{ij}dp_f; \quad d\sigma'_{ij} = D_{ijkl}d\varepsilon_{kl} \tag{3}$$

In above equations, σ_{ij} is the total Cauchy stress tensor (where $\sigma_{ij} > 0$ for tension) and b_i denotes the body force distribution vector; σ'_{ij} is the effective stress tensor; $\alpha = 1 - C_s/C_\phi$ is the Biot constant; C_s and C_ϕ are the compressibility of soil grain and soil skeleton, respectively; ε_{ij} is the strain tensor; p_f is the porous fluid pressure (where $p_f > 0$ for compression); $1/Q = (\alpha - n)C_s + n\beta_f$ describes the bulk stiffness of soil-fluid mixture, where β_f is the compressibility of fluid phase and n represents porosity; $k_{ij} = K_{ij}/\gamma_w$ where K_{ij} is the Darcy permeability coefficient and γ_w is the weight of porous fluid; D_{ijkl} is a fourth-order tensor describing the constitutive relation of soil skeleton; δ_{ij} represents the Kronecker delta ($\delta_{ij} = 0$ if $i \neq j$ and $\delta_{ij} = 1$ if $i = j$).

2.2 Spatial and temporal discretization of the governing equations

Equations (1)–(3), accompanied by initial and boundary conditions, define the strong form of porous model under quasi-static conditions. By applying spatial discretization, the weak form of governing equations can be obtained. In this study, the Finite Element Method (FEM) [32] is adopted for spatial approximations (as described by $\mathbf{u}(\mathbf{x}, t) = \mathbf{N}_u\mathbf{U}(t)$, $p_f(\mathbf{x}, t) = \mathbf{N}_p p_f(t)$, where $\mathbf{N}_u$ and $\mathbf{N}_p$ represent the spatial interpolation matrices for solid displacement and pore pressure, respectively; $\mathbf{U}$ and p_f are the nodal solid displacement vector and nodal pore pressure vector, respectively; $\mathbf{x}$ is the nodal coordinate vector). After spatial discretization, the well-known θ-method [2, 24] is applied for temporal discretization. Then, the following system of equations can be obtained:

$$\begin{bmatrix} 0 & -\mathbf{G} \\ \mathbf{G}^\mathrm{T} & \mathbf{S} + \theta\Delta t\mathbf{H} \end{bmatrix} \begin{bmatrix} \mathbf{U}^{i+1} \\ p_f^{i+1} \end{bmatrix} + \begin{bmatrix} \int_\Omega \mathbf{B}^\mathrm{T}\sigma' d\Omega \\ 0 \end{bmatrix}$$
$$= \begin{bmatrix} 0 & 0 \\ \mathbf{G}^\mathrm{T} & \mathbf{S} - (1-\theta)\Delta t\mathbf{H} \end{bmatrix} \begin{bmatrix} \mathbf{U}^i \\ p_f^i \end{bmatrix} + \begin{bmatrix} \mathbf{F}_u^{i+\theta} \\ \Delta t\mathbf{F}_p^{i+\theta} \end{bmatrix} \tag{4}$$

where θ is the integration parameter in the interval $0 \leq \theta \leq 1$; $\mathbf{B}$ stands for the strain matrix; σ' is the vector form of effective stress tensor σ'_{ij}; $\mathbf{F}_u^{i+\theta} = (1-\theta)\mathbf{F}_u^i + \theta\mathbf{F}_u^{i+1}$, $\mathbf{F}_p^{i+\theta} = (1-\theta)\mathbf{F}_p^i + \theta\mathbf{F}_p^{i+1}$; the superscripts i and $i+1$ denote, respectively, quantities evaluated at the start and end of the step; The permeability ($\mathbf{H}$), coupling ($\mathbf{G}$), compressibility ($\mathbf{S}$) matrices are defined as:

$$\mathbf{H} = \int_\Omega \nabla\mathbf{N}_p^\mathrm{T}\mathbf{k}\nabla\mathbf{N}_p d\Omega \tag{5a}$$

$$\mathbf{G} = \int_\Omega \mathbf{B}^\mathrm{T}\alpha\mathbf{m}\mathbf{N}_p d\Omega \tag{5b}$$

$$\mathbf{S} = \int_\Omega \mathbf{N}_p^\mathrm{T}(1/Q)\nabla\mathbf{N}_p d\Omega \tag{5c}$$

and $\mathbf{m}$ is the vector form of Kronecker delta δ_{ij} and $\mathbf{k}$ is the matrix form of k_{ij}.

The vectors $\mathbf{F}_u$ and $\mathbf{F}_p$ account for prescribed traction (τ) and flux (q) boundary conditions, as well as body forces ($\mathbf{b}$) and sources (a), respectively. $\mathbf{F}_u$ and $\mathbf{F}_p$ are derived as

$$\mathbf{F}_u = \int_{\Gamma_\tau} \mathbf{N}_u^\mathrm{T}\tau(t)d\Gamma + \int_\Omega \mathbf{N}_u^\mathrm{T}\mathbf{b}(t)d\Omega \tag{6a}$$

$$\mathbf{F}_p = \int_{\Gamma_q} \mathbf{N}_p^\mathrm{T}q(t)d\Gamma + \int_\Omega \mathbf{N}_p^\mathrm{T}a(t)d\Omega \tag{6b}$$

where Ω and Γ ($\Gamma = \Gamma_\tau \cup \Gamma_u = \Gamma_p \cup \Gamma_q$; where Γ_v indicates the part of the boundary in which the variable v is prescribed) stand for the domain and the boundary of porous model, respectively.

The θ-method is unconditionally stable if $\theta \geq 0.5$ [2]. For the case of $\theta = 0.5$, that is Crank-Nicolson method, the θ-method is second-order accurate. However, it may generate unwanted oscillations [27]. In this study, $\theta = 1$, corresponding to backward Euler scheme, is adopted, which is first-order accurate, unconditionally stable and can damp out spurious oscillations [28].

2.3 Evolution of compressibility of pore fluid in gassy sand

Due to the microstructure of sand, the gas bubbles are small and confined in the pore fluid, which have no impact on solid matrix. Accordingly, the gas–water mixture can be treated as a homogenous fluid, and it is reasonable to assume that the surface tension force of gas bubbles is negligible [7]. Consequently, the pore gas pressure is equal to the pore water pressure, and also equal to the gas–water mixture pressure. Based on the above hypothesis, Fredlund [7] combined the Boyle's law for dissolved gas and Henry's law for free gas, and then proposed the following equation for calculating the compressibility of miscible gas/fluid mixtures:

$$\beta_f = B_a(1 - S_r + hS_r)/(p_f + P_{atm}) + B_w S_r \beta_w \tag{7}$$

where B_a and B_w are the pressure parameters for pore gas and fluid, respectively; S_r stands for degree of saturation; h denotes the Henry's volumetric coefficient of solubility;

$P_{atm} = 101.3$ kPa is atmospheric pressure; β_w is the compressibility of pore water. In this study, pressure parameters B_a and B_w are both taken equal to 1.0. β_w can be taken as 4.7×10^{-7} kPa^{-1}. For the value of h, it varies for different gas–fluid mixtures. For example, $h = 0.034$ for methane (CH$_4$)-water mixtures; $h = 0.86$ for carbon dioxide (CO$_2$)–water mixtures; $h = 0.015$ for nitrogen (N$_2$)–water mixtures.

As shown in Eq. (7), the compressibility of pore fluid β_f is associated with degree of saturation S_r and pore fluid pressure p_f. The latter is one of the dependent variables of the porous model. For degree of saturation, its variation is very complex due to the drainage conditions and the distribution of bubble in the pore fluid. In this study, two cases, i.e. drained case and undrained case, are distinguished for determining S_r. For drained case, S_r is assumed constant during the consolidation process. For undrained case, through the differentiation of S_r, it can be obtained that

$$dS_r/S_r + dn/n + d\varepsilon_{ii} = 0 \tag{8}$$

By integrating Eq. (8), the evolution of S_r can be obtained as

$$S_r = \frac{S_{r0}n_0}{n} e^{-\Delta\varepsilon_{ii}} \tag{9}$$

where S_{r0} and n_0 are the initial degree of saturation and porosity. Obviously, the porosity n must be derived firstly for the calculation of S_r, which is also needed for the determination of $1/Q$ in Eq. (2). Based on the mass conservation of soil skeleton, the evolution of n can be obtained as [16]

$$\dot{n} + (\alpha - n)(\dot{\varepsilon}_{ii} + C_S\dot{p}_f) = 0 \tag{10}$$

If the compressibility of soil grain is not taken into account, i.e. $C_s = 0$ and $\alpha = 1.0$, which is reasonable for the most soil mechanics problem and adopted in this paper, porosity n can be derived by time integration as

$$n = 1 - (1 - n_0)e^{-\Delta\varepsilon_{ii}} \tag{11}$$

Above all, the pore fluid compressibility β_f is very sensitive to the presence of gas, and a small volume of bubbles can significantly affect the pore pressure response to external loading. For undrained case, due to the high compressibility of pore fluid, the application of external load on gassy soil brings about the change in its volume, which is accompanied with the gas dissolution or exsolution, as well as the variation of β_f. This volumetric deformation then leads to the variation of pore fluid pressure, and influences the effective stress–strain relationship.

2.4 Constitutive model

Since the gassy sand is considered as a saturated two-phase media with the liquid phase compressible, the effective stress concept for water fully saturated soil still applies to gassy sand. Accordingly, the constitutive model for water saturated sand can be used to analyse the stress–strain relationship of gassy sand.

It is widely known that the constitutive model plays the key role in numerical simulation of the soil response. In this paper, a sand model within the bounding surface plasticity theory and the critical state theory, named SANISAND-Z model [3], is adopted. The most attractive characteristic of the model is the omission of yield surface. That is the yield surface becomes identical to the stress point itself, so the direction of the plastic strain increment depends on the direction of the stress increment. These properties not only render the model incrementally non-linear, but also make the structure of the model simple. Furthermore, as results of the bounding surface plasticity and the introduction of state parameter, the model can simulate the mechanical behaviour of sand under monotonic and cyclic loading for a wide range of densities (loose and dense sands) and stress level with a single set of model parameters. For the sake of clearness, the constitutive ingredients of the model are summarized briefly.

As pointed out by Dafalias and Taiebat [3], zero elastic range does not negate the elastic deformations. The total strain is still decomposed into elastic and plastic strain. A hypoelastic model associated with shear moduli G and bulk moduli K is employed to describe the elastic behaviour:

$$G = G_0 \frac{(2.97 - e)^2}{1 + e} \left(\frac{p'}{P_{atm}}\right)^{0.5}; \quad K = \frac{2(1 + \mu)}{3(1 - 2\mu)}G \tag{12}$$

where $p' = \sigma_{ii}/3$ stands for the mean effective stress, e represents void ratio; G_0 is a model parameter; μ denotes a constant Poisson ratio.

For the critical state of soils, it can be described in triaxial $p' - q$ space and in $e - p$ space, i.e.

$$\eta = \frac{q}{p'} = M; \quad e = e_c = e_{ref} - \lambda\left(\frac{p'}{P_{atm}}\right)^\xi \tag{13}$$

where η represents the deviator stress ratio in triaxial space; $q = (3/2\boldsymbol{s} : \boldsymbol{s})^{1/2}$ is the deviator stress with the deviator stress tensor $\boldsymbol{s} = s_{ij} = \sigma_{ij} - \delta_{ij}p'$; M is a function of the Lode angle, called critical state stress ratio; e_c is the critical state void ratio; e_{ref}, λ, ξ are the model parameters.

In order to model the dilatancy of sand, the state parameter $\psi = e - e_c$ [1] is introduced in bounding surface (BS) $F^b = 0$ and dilatancy surface (DS) $F^d = 0$, which are given by

$$F^b = \left(\boldsymbol{r}^b : \boldsymbol{r}^b\right)^{1/2} - \sqrt{\frac{2}{3}}M^b = 0; \quad M^b = Me^{-n_b\psi} \quad (14)$$

$$F^d = \left(\boldsymbol{r}^d : \boldsymbol{r}^d\right)^{1/2} - \sqrt{\frac{2}{3}}M^d = 0; \quad M^d = Me^{n_d\psi} \quad (15)$$

where $\boldsymbol{r} = r_{ij} = s_{ij}/p'$ is the deviator stress ratio tensor; the superscripts b and d of $\boldsymbol{r}$ indicate the stress ratio on BS and DS, respectively; n_b and n_d are the model parameters. For simplicity, the value of M is taken as the average between its triaxial compression and extension values, M_c and M_e, respectively, to compensate for the exclusion of Lode angle dependence. So, the BS and DS in stress ratio π-plane are circles, as shown in Fig. 1.

The image stress point on BS can be determined in terms of the direction of the rate of stress ratio $\boldsymbol{r}$. To do this, two cases are distinguished, i.e. the current stress ratio $\boldsymbol{r}$ is inside or outside the BS. For the former case, as shown in Fig. 1, the image stress ratio point $\boldsymbol{r}^b$ can be analytically derived as

$$\boldsymbol{r}^b = -\boldsymbol{r}^t : \boldsymbol{v} + \left[\left(\boldsymbol{r}^t : \boldsymbol{v}\right)^2 + 2/3\left(M^b\right)^2 - \boldsymbol{r}^t : \boldsymbol{r}^t\right] \quad (16)$$

where $\boldsymbol{v} = d\boldsymbol{r}/(d\boldsymbol{r} : d\boldsymbol{r})^{1/2}$ stands for the direction of stress ratio rate; $d\boldsymbol{r} = \boldsymbol{r}^{t+1} - \boldsymbol{r}^t$ is the incremental tensor of stress ratio; $\boldsymbol{r}^t$ and $\boldsymbol{r}^{t+1}$ denote the previous and the current stress ratio tensor, respectively. For the latter case, that is $\boldsymbol{r}^{t+1}$ lies outside the BS, $\boldsymbol{r}^b$ is defined as the intersection with the BS of the radius connecting the origin to $\boldsymbol{r}^{t+1}$, also as shown in Fig. 1, which can be expressed by

$$\boldsymbol{r}^b = \sqrt{2/3}M^b\boldsymbol{n}^r \quad (16)$$

where $\boldsymbol{n}^r = \boldsymbol{r}^{t+1}/(\boldsymbol{r}^{t+1} : \boldsymbol{r}^{t+1})^{1/2}$ represents the direction of
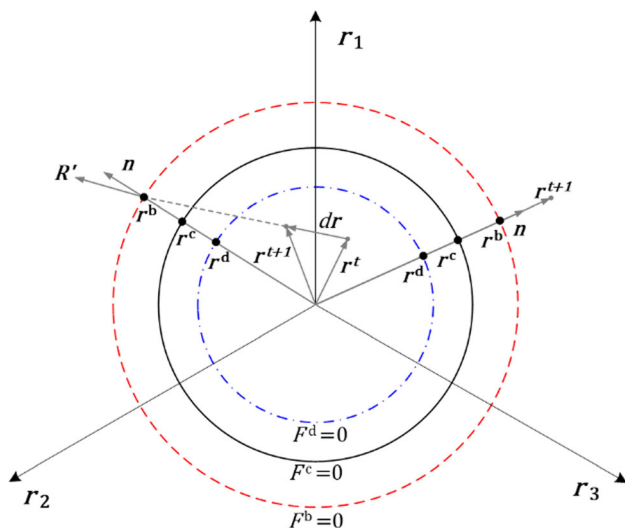

Fig. 1 Illustration of the SANISAND-Z model in deviator stress ratio space in conjunction with the bounding ($F^b = 0$), dilatancy ($F^b = 0$) and critical state ($F^c = 0$) surfaces (after [2])

$\boldsymbol{r}^{t+1}$. The loading direction $\boldsymbol{n}$ is defined normal to BS at $\boldsymbol{r}^b$, hence after the derivation of Eq. (14) one has

$$\boldsymbol{n} = \partial F^b/\partial \boldsymbol{r}^b = \boldsymbol{r}^b/\left(\boldsymbol{r}^b : \boldsymbol{r}^b\right)^{1/2} \quad (17)$$

and now, the stress point on DS $\boldsymbol{r}^d$ can be calculated as

$$\boldsymbol{r}^d = \sqrt{2/3}M^d\boldsymbol{n} \quad (18)$$

As for the direction of plastic strain, it can be decomposed into deviatoric part $\boldsymbol{R}'$ and volumetric part D in the model. The former is obtained by non-associative flow rule and is given by

$$\boldsymbol{R}' = B\boldsymbol{n} - C\left(\boldsymbol{n}^2 - \boldsymbol{I}/3\right); \quad B = 1 + \frac{3}{2}\frac{1-c}{c}g(\theta)\cos3\theta';$$

$$C = 3\sqrt{\frac{3}{2}\frac{1-c}{c}}g(\theta'); g(\Omega) = \frac{2c}{(1+c) - (1-c)\cos3\Omega};$$

$$c = M_e/M_c \quad (19)$$

where Ω is the Lode angle; M_e and M_c are the critical stress ratios in triaxial extension and compression. The volumetric part D is given by

$$D = A_d\left(\boldsymbol{r}^d - \boldsymbol{r}\right) : \boldsymbol{n} \quad (20)$$

where A_d is a model parameter. For the simplest case, A_d is constant. However, in order to take into account of the effect of fabric change on dilatancy, which is confirmed benefit for the simulation of liquefaction, A_d is related to a fabric-dilatancy tensor $\boldsymbol{z}$, i.e. $A_d = A_0\left(1 + \sqrt{3/2}\langle\boldsymbol{z} : \boldsymbol{n}\rangle\right)$ where the MacCauley bracket $\langle\rangle$ operates $\langle x\rangle = x$ for $x > 0$ and $\langle x\rangle = 0$ for $x \leq 0$; A_0 is a model constant; $\boldsymbol{z}$ evolves according to $\dot{\boldsymbol{z}} = -c_z - \dot{\varepsilon}_v^p\left(\sqrt{2/3}z_{max}\boldsymbol{n} + \boldsymbol{z}\right)$.

The last constitutive ingredient of the model is the plastic modulus K_p, which is expressed as

$$K_p = \frac{2}{3}p'h\frac{\left(\boldsymbol{r}^b - \boldsymbol{r}\right) : \boldsymbol{n}}{\left(\boldsymbol{r} - \boldsymbol{r}_{in}\right) : \boldsymbol{n}}; \quad h' = G_0h_0'(1 - c_he)\left(\frac{p'}{P_{atm}}\right)^{1/2} \quad (21)$$

where h_0' and c_h are the model parameters; $\boldsymbol{r}_{in}$ is the value of $\boldsymbol{r}$ at the initiation of a plastic loading.

Above all are the essential elements of the SANISAND-Z model. The model involves 14 material constants, as presented in Table 1. The calibration process for the model have been presented in detail by Dafalias and Taiebat [3], and is not elaborated here.

2.5 Numerical implementation

Numerical implementation of the above two-phase porous model is performed by using the user-defined element (UEL) interface provided by the FEM software Abaqus. In

Table 1 Material constants of the model

Parameters description	Symbol	Toyoura sand [23]	Baskarp sand [20]	Oakridge sand [22]	Ottawa sand [11]
Elasticity	G_0	125	150	100	50
	μ	0.05	0.1	0.15	0.25
Critical state	M_c	1.25	1.4	1.23	1.22
	c	0.712	0.712	0.712	0.713
	e_{ref}	0.934	0.886	1.417	0.8
	ξ	0.7	0.6	0.1	0.075
	λ	0.019	0.03	0.55	0.04
Dilatancy	A_0	0.704	0.457	0.420	1.487
	n_d	2.1	3.5	3.5	3.5
Plastic modulus	h'_0	15.0	8.1	2.1	6.9
	c_h	0.987	0.87	0.87	0.57
	n_b	1.25	1.1	2.1	1.1
Fabric-dilatancy tensor	z_{max}	2	–	–	–
	c_z	600	–	–	–

fact, two-phase porous model under quasi-static condition has been incorporated in Abaqus. However, the compressibility of liquid phase in the model is an input constant, which makes it unable to simulate the gassy soils behaviour, as described above. Due to the adoption of Newton–Raphson iterative method, two basic arrays, i.e. **AMATRX** and **RHS**, are required to be evaluated in the UEL subroutine, which represent the elemental stiffness matrix and the overall elemental residual, respectively. Utilizing Eq. (4) with $\theta = 1$, the **AMATRX** and **RHS** can be expressed as

$$
\mathbf{AMATRX} = \begin{bmatrix} \mathbf{K} & -\mathbf{G} \\ \mathbf{G^T}/\Delta t & \mathbf{S}/\Delta t + \mathbf{H} \end{bmatrix};
$$
$$
\mathbf{RHS} = \begin{bmatrix} G p_f^{i+1} - \int_\Omega \mathbf{B^T} \boldsymbol{\sigma}' d\Omega \\ -\mathbf{G^T}\dot{\mathbf{U}} - S\dot{p}_f - H p_f^{i+1} \end{bmatrix}
\tag{22}
$$

where $\mathbf{K} = \int_\Omega \mathbf{B^T} DB d\Omega$; $\dot{\mathbf{U}} = (\mathbf{U}^{i+1} - \mathbf{U}^i)/\Delta t$ and $\dot{p}_f = (p_f^{i+1} - p_f^i)/\Delta t$. In this study, the 3-D user-defined element is developed.

For the constitutive integration of the SANISAND-Z model, an implicit integration method is used. Based on the ingredients of the model, the Newton–Raphson iterative method is employed to solve the following system of nonlinear equations.

$$
\begin{cases}
\boldsymbol{\phi}_1 = \boldsymbol{s}^{t+1} - \boldsymbol{s}^t - 2G^{t+1}de + 2G^{t+1}L^{t+1}\boldsymbol{R}'^{t+1} = 0 \\
\phi_2 = p'^{t+1} - p'^t - K^{t+1}d\varepsilon_v + K^{t+1}L^{t+1}D^{t+1} = 0 \\
\phi_3 = 2G^{t+1}\boldsymbol{n}^{t+1} : de - K^{t+1}(\boldsymbol{n}^{t+1} : \boldsymbol{r}^{t+1})d\varepsilon_v \\
\quad -L^{t+1}\left(K_p^{t+1} + 2G^{t+1} - K^{t+1}D^{t+1}\boldsymbol{n}^{t+1} : \boldsymbol{r}^{t+1}\right) = 0
\end{cases}
\tag{23}
$$

where the superscripts t and $t+1$ represent the values of variables at the previous and current steps. After solving 8 unknown dependent variables of Eq. (23), i.e. six deviator stress components $\boldsymbol{s}^{t+1}$ (considering the symmetry of stress), p'^{t+1} and L^{t+1}, the corresponding tangent operator $\boldsymbol{D}$ consistent with the above stress update algorithm is derived as follows.

By deriving Eq. (23) with respect to the strain tensor $\boldsymbol{\varepsilon}$, one has

$$
\begin{bmatrix} \dfrac{d\phi_1}{d\boldsymbol{\varepsilon}} \\ \dfrac{d\phi_2}{d\boldsymbol{\varepsilon}} \\ \dfrac{d\phi_3}{d\boldsymbol{\varepsilon}} \end{bmatrix} = \begin{bmatrix} \dfrac{\partial\phi_1}{\partial\boldsymbol{\varepsilon}} \\ \dfrac{\partial\phi_2}{\partial\boldsymbol{\varepsilon}} \\ \dfrac{\partial\phi_3}{\partial\boldsymbol{\varepsilon}} \end{bmatrix} + \boldsymbol{J} \begin{bmatrix} \dfrac{\partial\boldsymbol{s}}{\partial\boldsymbol{\varepsilon}} \\ \dfrac{\partial p'}{\partial\boldsymbol{\varepsilon}} \\ \dfrac{\partial L}{\partial\boldsymbol{\varepsilon}} \end{bmatrix} = 0;
$$
$$
\boldsymbol{J} = \begin{bmatrix} \dfrac{\partial\phi_1}{\partial\boldsymbol{s}} & \dfrac{\partial\phi_1}{\partial p'} & \dfrac{\partial\phi_1}{\partial L} \\ \dfrac{\partial\phi_2}{\partial\boldsymbol{s}} & \dfrac{\partial\phi_2}{\partial p'} & \dfrac{\partial\phi_2}{\partial L} \\ \dfrac{\partial\phi_3}{\partial\boldsymbol{s}} & \dfrac{\partial\phi_3}{\partial p'} & \dfrac{\partial\phi_3}{\partial L} \end{bmatrix}
\tag{24}
$$

The operator $\boldsymbol{J}$ has been determined in advance when iteratively solving Eq. (23). Then, after some tensor algebra and inversion, one can obtain $\partial\boldsymbol{s}/\partial\boldsymbol{\varepsilon}$ and $\partial p'/\partial\boldsymbol{\varepsilon}$. Finally, the consistent tangent operator can be given by

$$
\boldsymbol{D} = \frac{\partial\boldsymbol{\sigma}}{\partial\boldsymbol{\varepsilon}} = \frac{\partial\boldsymbol{s}}{\partial\boldsymbol{\varepsilon}} + \boldsymbol{I} \otimes \frac{\partial p'}{\partial\boldsymbol{\varepsilon}}
\tag{25}
$$

where $\boldsymbol{I}$ is the second-order unit tensor; $\otimes$ denotes tensor product.

3 Evaluation of the numerical model

In order to validate the proposed numerical porous model, the numerical element tests are conducted and their results are then compared with the experimental data. In this process, the water fully saturated condition and the gas-bearing condition are both investigated. The former is mainly for demonstrating the accuracy of the numerical implementation of the porous model, and the latter is primarily for confirming the capabilities of the model against gassy sand.

3.1 Simulations of water fully saturated sand

The experimental data of Toyoura sand published by Verdugo and Ishihara [23] are employed for validation, including the drained and undrained triaxial compression testing results. This sand is a uniform fine sand consisting of subrounded to subangular particles. The mean diameter and the uniformity coefficient are 0.17 mm and 1.7, respectively. The maximum and minimum void ratio are 0.977 and 0.597, respectively. The material parameters of the SANISAND-Z model is presented in Table 1, which is from Dafalias and Taiebat [3]. In the simulations of triaxial compression tests on the water fully saturated sand and the following gassy sands, the critical stress ratio M is set equal to the compression value M_c. It should be noted that due to the discontinuity of Eq. (7) at $S_r = 1$, i.e. the fully saturated condition, the compressibility of the pore fluid should be directly taken as 4.7×10^{-7} kPa^{-1}.

Figure 2 illustrates the isotropically consolidated drained (CID) triaxial compression testing data (Fig. 2a, b) and the simulations of the model (Fig. 2c, d). The experiments cover two confining pressure levels (100 kPa and 500 kPa) and a wide range of initial void ratio e_0 (0.810–0.996). It can be calculated from the second formula of Eq. (13) that, the critical void ratio e_c is equal to 0.915 and 0.875 for $p' = 100$ kPa and $p' = 500$ kPa, respectively. It

then can be observed that the stress–strain relations are softening types with volumetric dilation for dense sand (state parameter $\psi_0 = e_0 - e_c < 0$), while the stress–strain relations are hardening types with volumetric contraction for loose sand ($\psi_0 > 0$). For a given confining pressure, the critical states corresponding to different e_0 are approximately identical. The simulations of the model match the observed behaviour very well.

Figure 3 illustrates the isotropically consolidated undrained (CIU) triaxial compression testing data (Fig. 3a, b) and the simulations of the model (Fig. 3c, d). The experiments cover a wide range of confining pressure (from 100 to 3000 kPa) and initial void ratio e_0 (0.735–0.907). Similar with the drained behaviour, variations of undrained triaxial compression response from highly dilatant to highly contract can also be observed depending on the value of state parameter. For a given e_0, the critical states corresponding to different confining pressures are approximately identical. Again, the predicted and observed results are found to agree well.

Above all, the close matching of the physical testing data with the numerical simulations represents a satisfactory validation of numerical implementation of the proposed porous model. In the next section, the mechanical behaviour of gassy sands with different physical state will be investigated by the proposed numerical model.
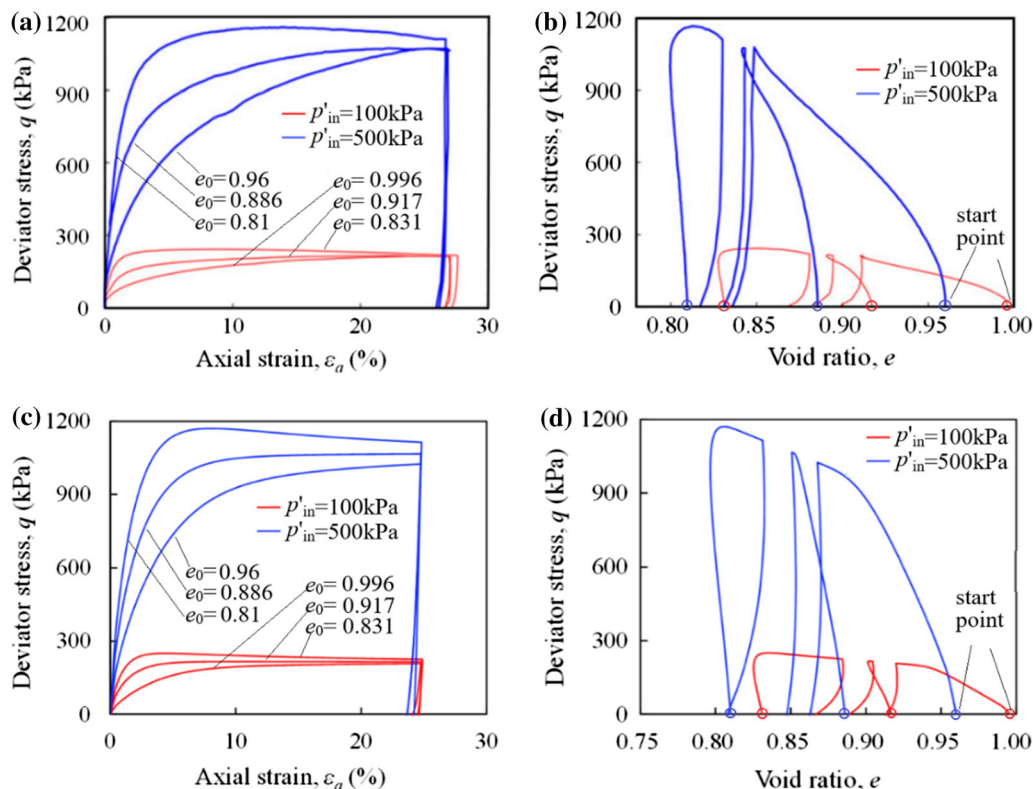

Fig. 2 Simulations compared with CID triaxial compression testing data: **a**, **b** experimental data (after [23]); **c**, **d** simulated results
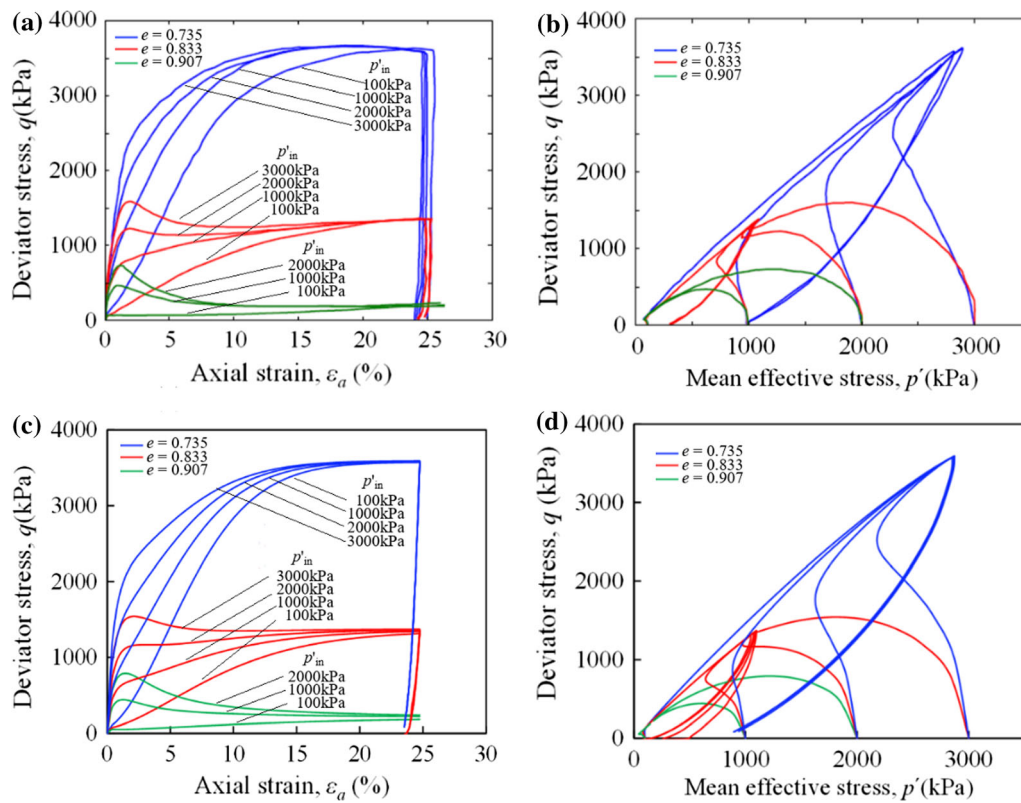
Fig. 3 Simulations compared with CIU triaxial compression testing data: **a**, **b** experimental data (after [23]); **c**, **d** simulated results

3.2 Simulations of gassy sand

As experimentally investigated by previous researchers, the gassy sand behaviour is significantly influenced by many factors, such as the gas type, gas amount, pore fluid pressure as well as the physical state of sand. In this section, the effects of these factors are studied using the proposed porous model. The published experimental results, including undrained triaxial compression tests on dense gassy Baskarp sand [20], dense gassy Oakridge sand [22] and loose gassy Ottawa sand [11], are employed to verify the proposed numerical model. The parameters of SANI-SAND-Z model for each sand are listed in Table 1. For simplicity, the effect of fabric change in dilatancy is not taken into account for each simulation of gassy sand. The model parameter A_d is constant and equal to A_0, so the parameters z_{max} and c_z are not provided. In addition, an additional model parameter, i.e. Henry's volumetric coefficient of solubility h, is needed for the simulations.

The experimental data by Rad et al. [20] are utilized to examine the effects of gas type, gas amount and pore fluid pressure level. A series of CIU triaxial compression tests on gassy and saturated samples of Baskarp sand, as well as CID triaxial compression tests on saturated samples, were performed. The relative density D_r for each sample was about 85%. The confining pressure was set to be 50 kPa.

Baskarp sand is a fine river sand. The maximum and minimum void ratio is 0.86 and 0.503, respectively. The specific gravity is 2.65.

For the effect of gas type (CO_2 and CH_4) on the dense gassy sand behaviour, Fig. 4a–c shows the comparisons between the measured and predicted responses of the deviator stress q, pore fluid pressure p_f and volumetric strain ε_v (negative value for expansion) with axial strain ε_a, respectively. Since the corresponding effective stress path was not directly presented in [20], only the prediction results are provided in Fig. 4d. These figures demonstrate that: (i) during the early stage, because the gas is dissolved in the pore fluid, the variations of deviator stress, pore fluid pressure and volumetric strain, as well as the effective stress path for gassy sands induced by shear contraction are almost the same as the ones of water fully saturated sand. This behaviour is more clearly shown in Fig. 5; (ii) in the later stage, the shear dilation of dense sand leads to gas exsolution, then the responses of gassy sand become quite distinct from the water saturated sand owing to the significant increase in the compressibility of pore fluid. The effective stress paths of gassy sand gradually deviate from that of saturated undrained case. The response curves of the gassy sand lie between the reference drained and undrained testing results, showing partial (internal) drainage characteristic even under undrained condition; (iii) the more
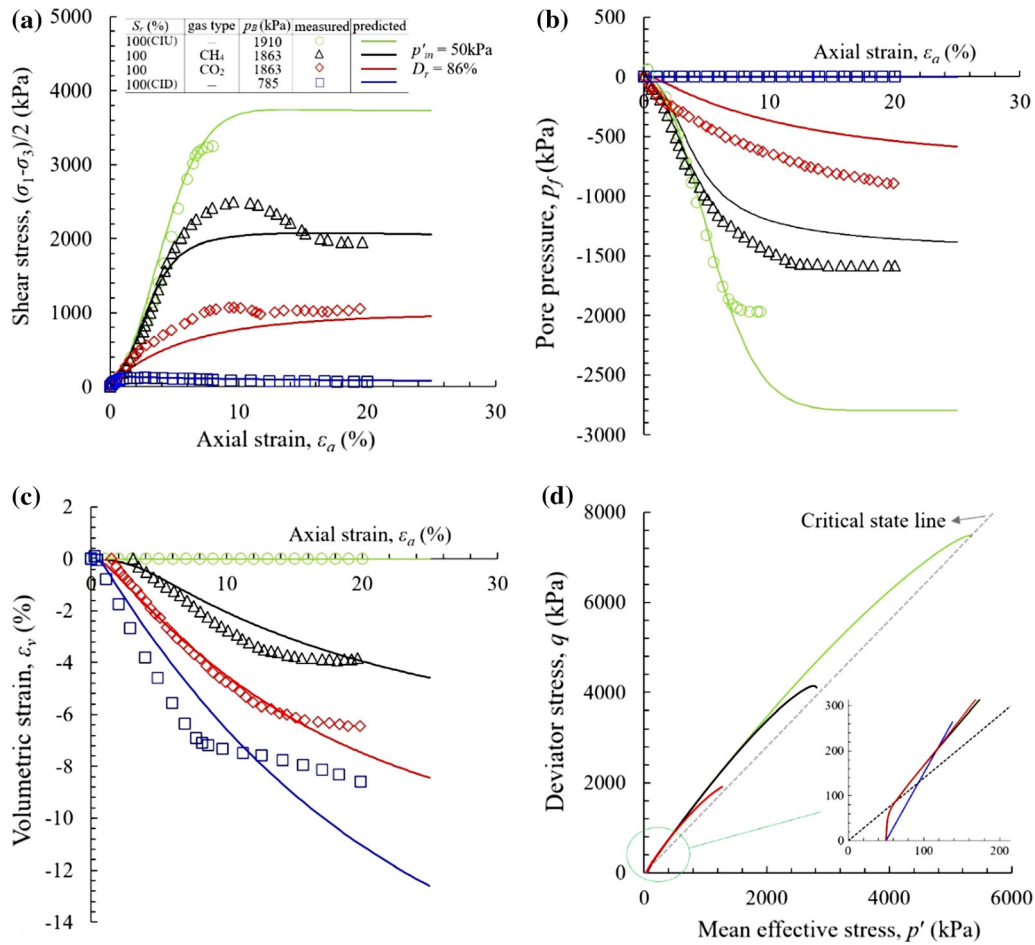
Fig. 4 Simulations compared with experimental data from undrained triaxial tests by Rad et al. [20] considering the effect of gas type: **a** $q/2$ versus ε_a; **b** p_f versus ε_a; **c** ε_v versus ε_a; **d** effective stress path
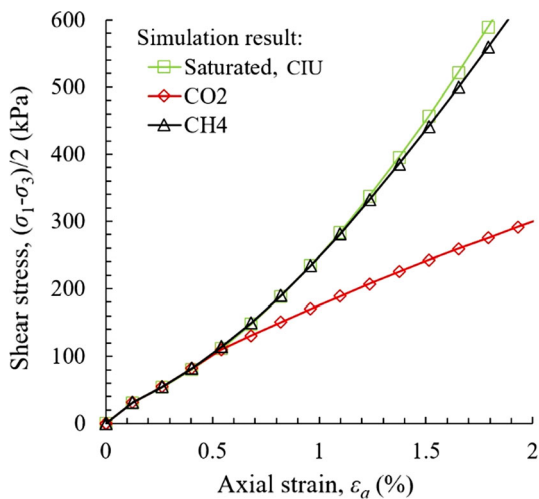

Fig. 5 Simulations of deviator stress against axial strain under small scale

soluble the gas (i.e. CO_2 relative to CH_4) is, the stronger the gas exsolution and the subsequent volumetric expansion will be, thus the less intense the pore pressure

reduction and the lower the undrained shear strength will be; (iv) in triaxial $p - q$ space, the effective stress paths for gassy and saturated sand tend to arrive at an identical critical state line; (v) the predictions are comparable with the experimental results, indicating that the effects of gas-bearing, gas type, and the dilatancy of gassy sand can be well captured by the proposed numerical model.

To reveal the effect of gas amount on the undrained static behaviour of gassy sand, two specimens with initial degree of saturation S_{r0} equal to 90% (gas in free form) and 100% (gas in solution) were compared. The used gas type is CH_4. Figure 6a–c compare the measured and predicted curves of $q - \varepsilon_a$, $p_f - \varepsilon_a$ and $\varepsilon_v - \varepsilon_a$. Figure 6d shows the simulated effective stress paths. As shown by the test data, due to the more pore fluid pressure reduction in the gassy sand specimen with $S_{r0} = 100\%$ during the early loading stage, it exhibits a higher peak shear strength than the one with $S_{r0} = 90\%$. With the gas exsolution resulting from shear dilation of dense sand, the residual strength and the pore fluid pressure become somewhat similar for the two gassy sand specimens. Evidently, the impact of gas amount
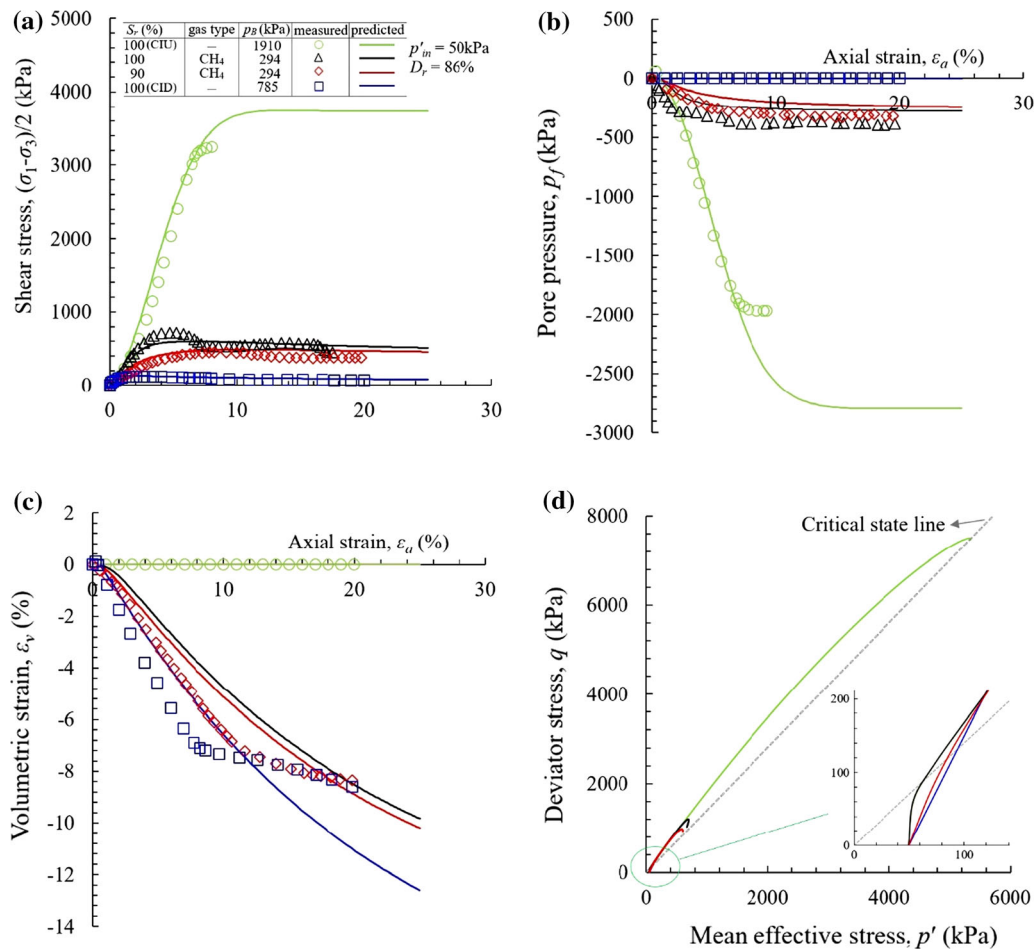
Fig. 6 Simulations compared with experimental data from undrained triaxial tests by Rad et al. [20] considering the effect of gas amount: **a** $q/2$ versus ε_a; **b** p_f versus ε_a; **c** ε_v versus ε_a; **d** effective stress path

on the peak and residual strength, the development of excess pore pressure and the volumetric strain can be reasonably described by the proposed numerical model. For the gassy specimen with $S_{r0} = 90\%$, the effective stress path in the initial loading stage is located between the saturated undrained and drained results because of the existence of free gas, then follows the saturated undrained results and finally reaches a different critical state from that of saturated undrained specimen.

As can be understood from Eq. (7) that the lower the pore fluid pressure is, the higher the compressibility of pore fluid will be. The variations of pore fluid pressure are bound to affect the behaviour of gassy sand. To study this effect, two gassy specimens with different initial pore fluid pressures p_B (of 441 kPa and 1863 kPa) were tested. The used gas was CO_2, which was fully dissolved in water with $S_r = 100\%$ for the two tests. The test results are summarized in Fig. 7a–c, in which the corresponding simulation results are also provided. Figure 7d shows the simulated effective stress paths. These figures clearly show that the higher the initial pore pressure is, the more intense the pore pressure

reduction thus the higher undrained shear strength will be. Meanwhile, the specimen with lower p_B can experience more volumetric deformation due to the higher compressibility of pore fluid. Those exhibited undrained static responses of gassy sand under different initial pore fluid pressures can be well predicted by the proposed numerical porous model.

The above experimental investigations by Rad et al. [20] are carried with respect to gassy dense sand. Besides, the study of impact of gas amount is relatively insufficient owing to the minor difference between the results of the merely two tests. To this end, the results of other two sets of undrained triaxial compression tests conducted on loose and dense sand are employed for further understanding of the effect of gas amount on the behaviour of gassy dense sand, and evaluating the influence of physical state of gassy sand on its static response.

Vega-Posada et al. [22] carried out a series of anisotropically consolidated undrained (CAU) triaxial compression tests on saturated and gassy dense sand. The sand was collected from the Oakridge waste disposal site
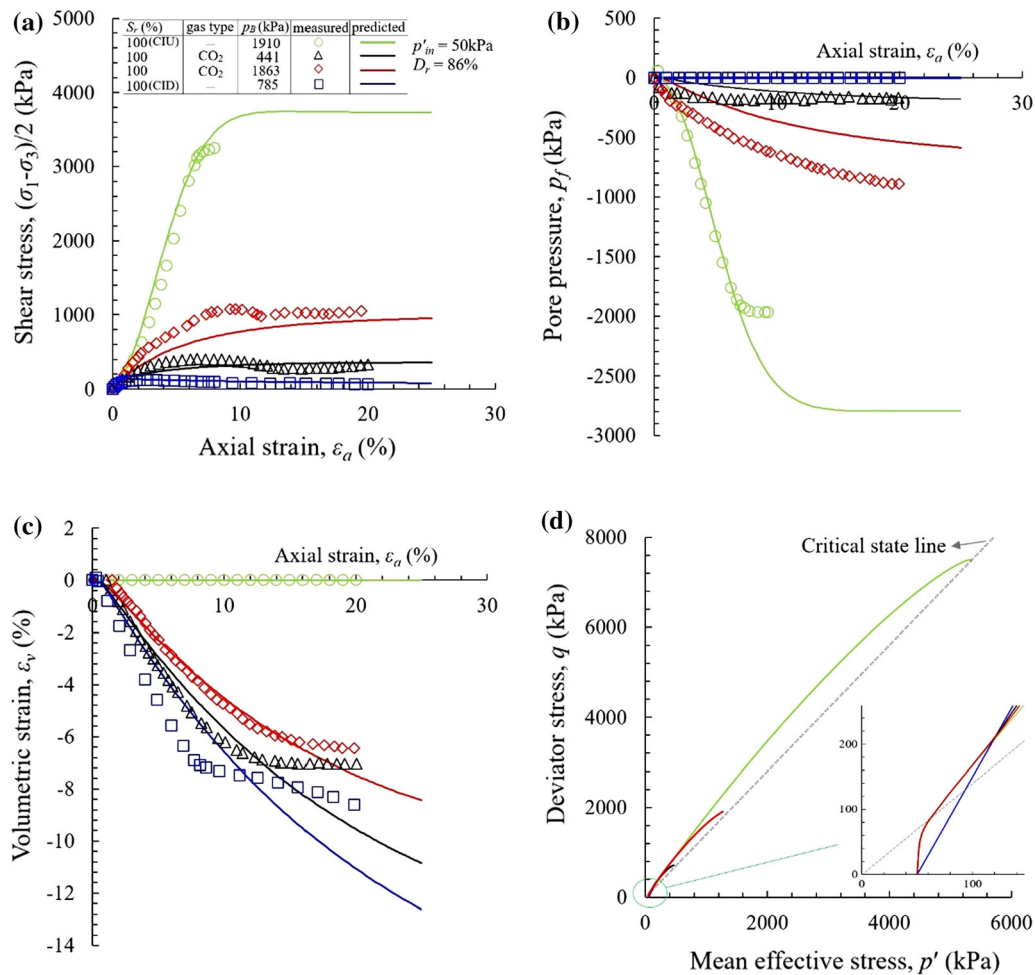
Fig. 7 Simulations compared with experimental data from undrained triaxial tests by Rad et al. [20] considering the effect of pore pressure: **a** $q/2$ versus ε_a; **b** p_f versus ε_a; **c** ε_v versus ε_a; **d** effective stress path

near Charleston, South Carolina. It is a uniform fine sand. The average uniformity coefficient and curvature coefficient are 1.63 and 1.03, respectively. The minimum and maximum void ratios are 0.62 and 1.05, respectively. The average initial void ratio of specimens is 0.71. The used gas for the gassy sand specimens was CO_2. The degree of saturation ranges from 75 to 98%. The initial deviator stress and mean effective stress are 54 kPa and 100 kPa for all specimens, respectively. The experimental results and the simulations of the model, including deviator stress, excess pore pressure and volumetric strain against axial strain as well as effective stress path in p'-q space, are illustrated in Fig. 8a–d. The reference drained and undrained (using water fully saturated specimen) test results are also provided in the figures. It is clear that the existence of gas presents a remarkable detrimental effect on the undrain shear strength of gassy dense sand. The stress–strain relationships for gassy sand specimens are similar to that of drained specimen, even if the initial gas amount is small. Combined with the experimental results

by Rad et al. [20], it can be concluded that the effect of gas amount on the undrained static response of gassy sand is minor if the gases are in free form. Besides, owing to the gas exsolution resulted from shear dilation of dense sand, the development of negative pore pressure is significantly suppressed. Correspondingly, the evolutions of volumetric strain and effective stress path exhibit a partially drained responses. The comparison between the measurements and predictions indicates that the above behaviour of gassy dense sand can be well described by the proposed numerical model.

Compared with gassy dense sand, laboratory data with respect to gassy loose sand under monotonic loading are less reported in literature. To study the desaturation for the mitigation of liquefaction of sand, He and Chu [11] conducted a series of isotropically consolidated undrained triaxial compression tests on loose Ottawa sand (relative densities $D_r \approx 10\%$) desaturated using nitrogen. The mean diameter of the tested sand is 0.4 mm. The maximum and minimum void ratio is 0.8 and 0.5, respectively. The degree
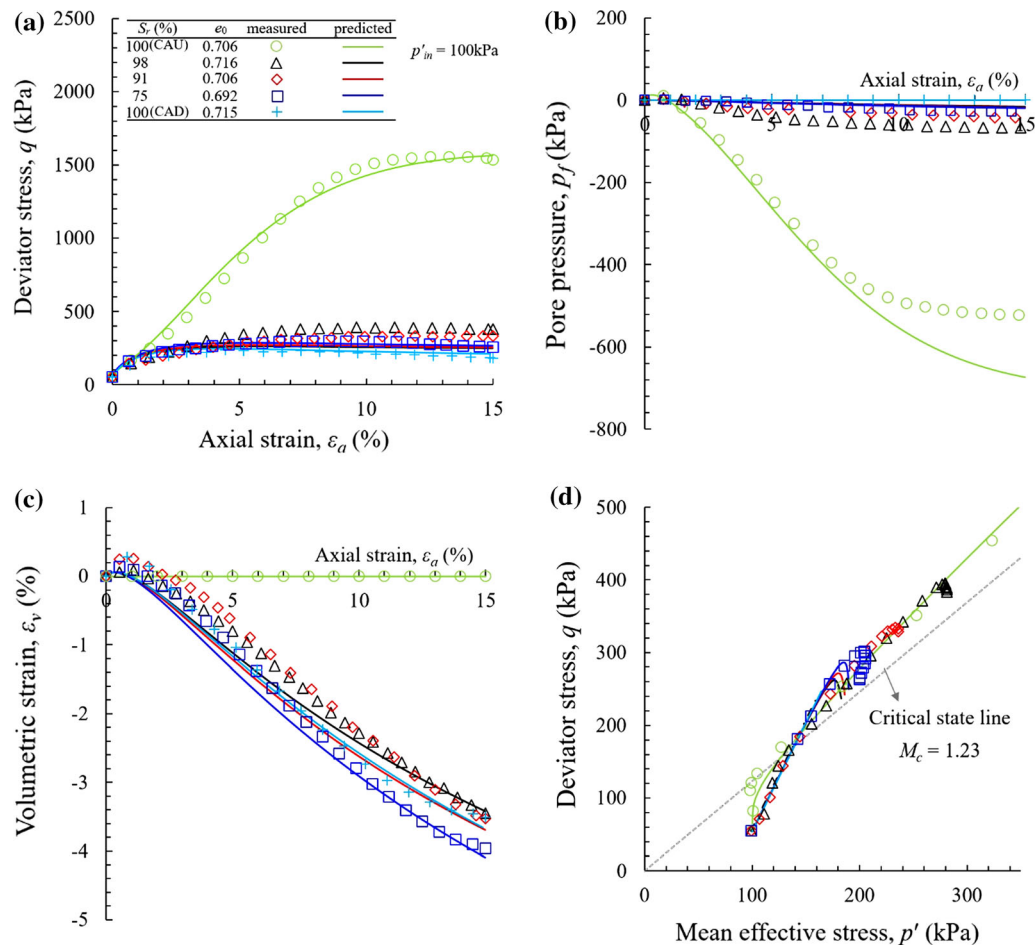
Fig. 8 Simulations compared with experimental data from undrained triaxial tests on dense gassy sand by Vega-Posada et al. [22]: **a** q versus ε_a; **b** p_f versus ε_a; **c** ε_v versus ε_a; **d** effective stress path

of saturation of the tested specimens ranged from 94.5% to 100%. The initial mean effective stress and the back pressure were 100 kPa for all tests. Figure 9a–d illustrates the measured data and the predicted results, including the deviator stress-axial strain relationships, the pore pressure—axial strain relationships and the effective stress paths in—$p'q$ space, as well as the variation of degree of saturated with deviator stress (only predicted results presented). It can be observed that the existence of gas plays an obvious benefit effect on the undrained shear strength of gassy loose sand, which is different from the responses of gassy dense sand. The peak deviator stresses of gassy specimens are higher than the one of water saturated specimen, and increase with the decrease in the degree of saturation. Meanwhile, the maximum pore water pressure becomes much smaller with the decrease in the degree of saturation. The reason behind is that gas dissolution resulted from the shear contraction of loose sand, and consequently partial (internal) drainage (reflected by the gradual increase of degree of saturation during the undrained loading, as shown in Fig. 9d), results in less

intense pore pressure increase (as shown in Fig. 9b), and thus the higher undrained peak strength. The effective stress paths of gassy sand are bounded by those of saturated undrained and drained conditions. It is found that the predictions are comparable with the experimental results, indicating that the proposed numerical model can be well capture the behaviour of gassy loose sand.

4 Conclusion

In this paper, the mechanical behaviour of gassy sand under monotonic loading conditions is numerically studied. The model parameters for the Toyoura sand are used for all gassy sand simulations, focusing on investigating the influence mechanism of different factors. The following conclusions can be drawn:

(1) By considering the gas–water mixture in gassy sand as homogenous pore fluid, a porous model is proposed for gassy sand based on the two-phase
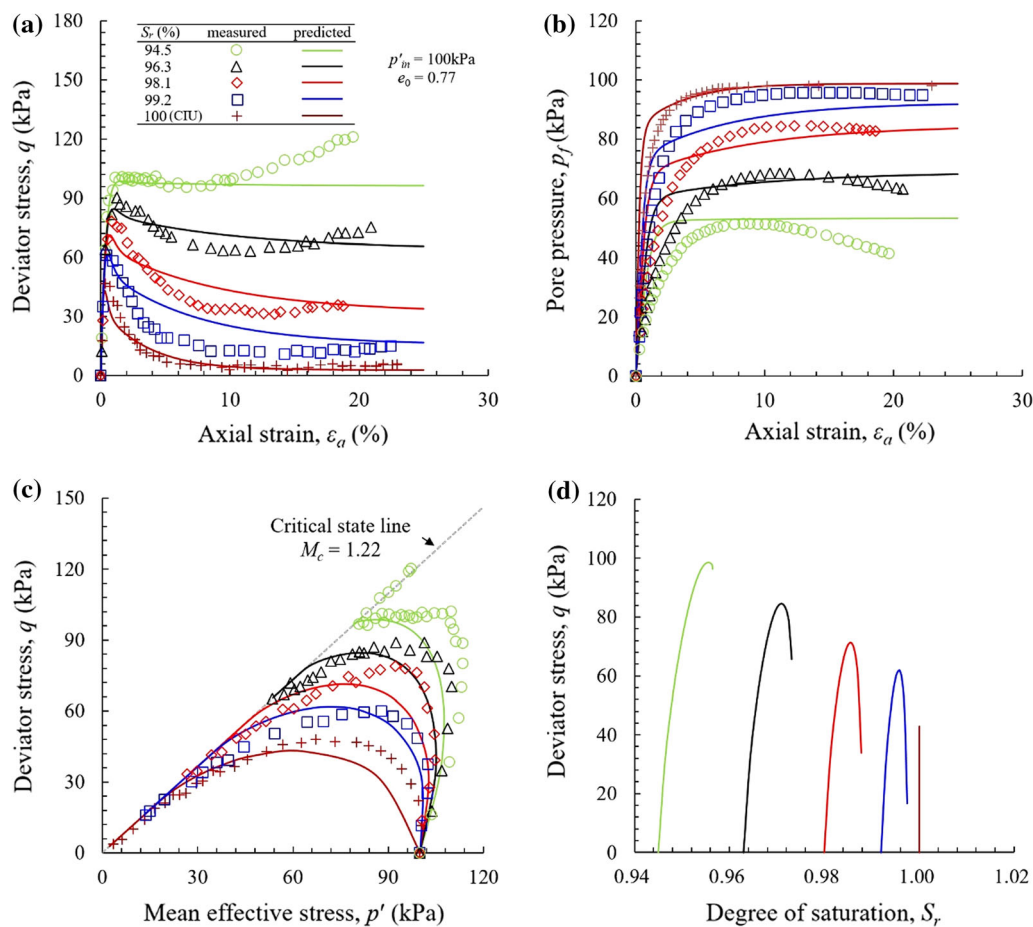
Fig. 9 Simulations compared with experimental data from undrained triaxial tests on loose gassy sand by He and Chu [11]: **a** q versus ε_a; **b** p_f versus ε_a; **c** effective stress path; **d** q versus S_r

saturated porous media theory. An advanced constitutive model, named SANISAND-Z model, is included for capturing the complex stress–strain behaviour of sand with only one set of model parameters. The effect of gas-bearing is described by the Boyle's and Henry's Laws, where the Henry's volumetric coefficient of solubility is introduced as a new material constant.

(2) The proposed porous is numerically implemented by the use of user-defined element (UEL) interface provided by the FEM software Abaqus. An implicit method is employed for the constitutive integration. The consistent tangent operator is also derived. The accuracy of the numerical implementation of the porous model is validated by the close matching of the physical testing results under fully water saturated cases with the constitutive simulations.

(3) Multiple influence factors of the quasi-static responses of gassy sand, including gas type, gas amount, and existing form of gas, pore pressure level as well as physical state (void ratio and stress level)

of sand, are investigated by the proposed numerical porous model. Due to the higher compressibility of pore fluid resulting from the presence of gas, the undrained static responses of gassy sand are bounded by the ones under fully saturated drained and undrained conditions. The measured responses of gassy sand under different factors concerned can be well reproduced by the proposed numerical porous model.

References

1. Been K, Jefferies MG (1985) A state parameter for sands. Géotechnique 35(2):99–112

2. Booker JR, Small JC (1975) An investigation of the stability of numerical solutions of Biot's equations of consolidation. Int J Solids Struct 11:907–917

3. Dafalias YF, Taiebat M (2016) SANISAND-Z: zero elastic range sand plasticity model. Géotechnique 66(12):999–1013

4. Dittrich JP, Rowe RK, Becker DE, Lo KL (2010) Influence of exsolved gases on slope performance at the Sarnia approach cut to the St. Clair Tunnel. Can Geotech J 47(9):971–984

5. Finno RJ, Zhang Y, Buscarnera G (2017) Experimental validation of Terzaghi's effective stress principle for gassy sand. J Geotech Geoenviron Eng 143(12):04017092

6. Fleischer P, Orsi TH, Richardson MD, Anderson AL (2001) Distribution of free gas in marine sediments: a global overview. Geo-Mar Lett 21(2):103–122

7. Fredlund DG (1976) Density and compressibility characteristics of air–water mixtures. Can Geotech J 13(4):386–396

8. Grozic JLH, Robertson PK, Morgenstern NR (1999) The behavior of loose gassy sand. Can Geotech J 36(3):482–492

9. Grozic JLH, Imam SMR, Robertson PK, Morgenstern NR (2005) Constitutive modeling of gassy sand behaviour. Can Geotech J 42(3):812–829

10. Grozic JLH, Nadim F, Kvalstad TJ (2005) On the undrained shear strength of gassy clays. Comput Geotech 32(7):483–490

11. He J, Chu J (2014) Undrained responses of microbially desaturated sand under monotonic loading. J Geotech Geoenviron Eng 140(5):04014003

12. Hilf JW (1948) Estimating construction pore pressures in rolled earth dams. In: Proceedings of the 2nd international conference on soil mechanics and foundation engineering, Rotterdam, Netherlands, vol 3, pp 234–240

13. Hong JT, Xu M (2020) DEM study on the undrained mechanical behavior of gassy sand. Acta Geotech 15(6):2179–2193

14. Hong Y, Wang LZ, Ng CW, Yang B (2017) Effect of initial pore pressure on undrained shear behaviour of fine-grained gassy soil. Can Geotech J 54(11):1592–1600

15. Imam SMR, Robertson PK, Chan DH, Morgenstern NR (2005) A critical-state constitutive model for liquefiable sand. Can Geotech J 42(3):830–855

16. Lewis RW, Schrefler BA (1998) The finite element method in the static and dynamic deformation and consolidation of porous media. Wiley, London

17. Mabrouk A, Rowe RK (2011) Effect of gassy sand lenses on a deep excavation in a clayey soil. Eng Geol 122(3–4):292–302

18. Niemunis A, Herle I (1997) Hypoplastic model for cohesionless soils with elastic strain range. Mech Cohesive-Frict Mater 2(4):279–299

19. Nixon MF, Grozic JL (2007) Submarine slope failure due to gas hydrate dissociation: a preliminary quantification. Can Geotech J 44(3):314–325

20. Rad NS, Vianna AJD, Berre T (1994) Gas in soil. II: effect of gas on undrained static and cyclic strength of sand. J Geotech Eng 120(4):716–736

21. Sobkowicz JC, Morgenstern NR (1984) The undrained equilibrium behaviour of gassy sediments. Can Geotech J 21(3):439–448

22. Vega-Posada CA, Finno RJ, Zapata-Medina DG (2014) Effect of gas in the mechanical behavior of medium dense sands. J Geotech Geoenviron Eng 140(11):04014063

23. Verdugo R, Ishihara K (1996) The steady state of sandy soils. Soils Found 36(2):81–91

24. Vermeer PA, Verruijt A (1981) An accuracy condition for consolidation by finite elements. Int J Numer Anal Methods Geomech 5:1–14

25. Von Wolffersdorff PA (1996) A hypoplastic relation for granular materials with a predefined limit state surface. Mech Cohesive-Frict Mater 1(3):251–271

26. Wheeler SJ (1988) A conceptual model for soils containing large gas bubbles. Géotechnique 38:389–397

27. Wood WL, Lewis RW (1975) A comparison of time marching schemes for the transient heat conduction equation. Int J Numer Methods Eng 9(3):679–689

28. Wood WL (1990) Practical time stepping schemes. Clarendon Press, Oxford

29. Wroth CP, Houlsby GT (1985) Soil mechanics: property characterization and analysis procedures. In: Proceedings of XI international conference on soil mechanics and foundation engineering, San Francisco, CA, pp 1–55

30. Xu M, Song EX, Jiang H, Hong JT (2016) DEM simulation of the undrained shear behavior of sand containing dissociated gas hydrate. Granul Matter 18(4):79

31. Zapata-Medina DG, Vergara CY, Vega-Posada CA, Arboleda-Monsalve LG (2019) on the use of Fredlund gas/fluid compressibility relationship to model medium-dense gassy sand behavior. Can Geotech J 56(8):1070–1079

32. Zienkiewicz OC, Taylor RL (2005) The finite element method, vol 2, 6th edn. Butterworth-Heinemann, Oxford